Aerodynamic Mapping of a Formula Student Prototype using Numerical Simulations and On-track Validation

Miguel Marques Carreira

miguel.carreira@tecnico.ulisboa.pt

Instituto Superior Técnico, Universidade de Lisboa, Portugal

June 2022

Abstract

Aerodynamic forces on a race car depend on its attitude, which changes along the track given the accelerations they are subjected to. The main objective of this work is to understand how these attitude changes affect the FST10e prototype aerodynamics. The car's attitude was broken down into five parameters of interest: front and rear ride heights, roll, steering and yaw angles, with the vehicle behaviour being estimated by CFD simulations. The primary focus of CFD was cornering condition simulation, with the corresponding numerical error estimated by performing a mesh convergence. The influence of each of these parameters was evaluated individually, revealing some unexpected results, with the most impactful sensitivity being the yaw angle with a 16% change in downforce across the interval. An aerodynamic map was then created based on over 100 data points, which provided a thorough understanding across the whole working envelope. The results can be promptly obtained by using a surrogate model, which overcomes the slow CFD analyses. Lastly, an aerodynamic validation component was also addressed to estimate downforce and drag coefficients with on-track testing. The main challenge encountered was to estimate air speed during validation testing, which revealed to be a great source of uncertainty to correlate CFD with track results.

Keywords: CFD, Formula Student, Aerodynamic mapping, On-track validation, Ride height, Vehicle attitude

1. Introduction

The aim of race cars is ultimately to win races and to do so, there are many areas where it is possible to reduce lap times and beat the competitors. Aerodynamics plays an important role in the vehicle's stability and handling [1], helping the driver to achieve consistent and quick lap times. As the car is in constant motion due to the accelerations it is subjected to (laterally when cornering and longitudinally when accelerating/braking) vehicle's attitude varies a lot across the track. These changes in the vehicle state directly affect the car aerodynamic performance and this work intends to understand how the aerodynamic forces and moments acting on a race car vary over a range of attitudes.

The understanding of this behaviour helps to understand in which conditions the aerodynamic package can be improved in the future but is also advantageous for vehicle dynamics understanding. It provides information to help identify zones of interest to ride the car in and adjust the car setup to ride on those conditions, reaching the full potential of the prototype. It is also possible to draw conclusions about the stability and "feeling" of the car that can help identify reasons for understeer or oversteer experienced by the driver. Aerodynamic forces are generated from distributed loads in different components across the car. In race cars, particularly in formulas, some typical aerodynamic devices are front and rear wing, sidepods and a floor/diffuser. This work focus on FST10e prototype, the 10th prototype made by FST Lisboa that is a Formula Student [2] competing team from Instituto Superior Técnico. Figure 1 describes the different components of the aerodynamic package of FST10e prototype.
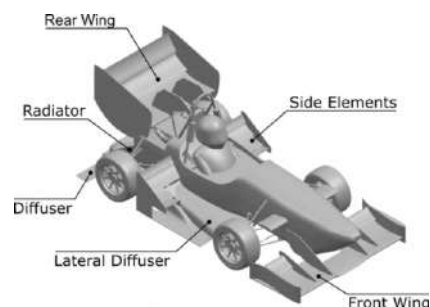

Figure 1: FST10e components

2. Background

2.1. Parameters of Interest

The car's attitude is represented by five different variables, each of them with a different impact on the aerodynamic behaviour.

The first parameter of interest for this study is ride height, which is divided into two ground clearances, front and rear (FRH and RRH respectively). As the prototype is close to the ground, ground effect is present and its impact changes depending on the distance to the ground [3]. As the axis are independent, it is divided into front and rear which also define the vehicle's pitch angle θ. Roll angle ϕ is the third variable taken into account and is also associated with changing ground clearance differentiating the distance from one side to another. This angle is a result of the car's lateral acceleration. The steering angle δ is also a parameter of interest since the wheel wake changes depending on δ [4]. As FST10e is an open wheel prototype, this wake affects upstream components. The steering angle was coupled with the cornering radius. The last variable considered for this study is yaw angle ψ which changes based on side-slip angle β and wind speed/angle. The ψ angle modifies the incoming airflow direction therefore it was considered to change the aerodynamic behaviour.

2.2. Variables of Interest

To study the effects of aerodynamics in vehicle dynamics, six variables were studied. Three force components are evaluated (x, y, z) and also the moments in all three directions. Forces are represented in a coefficient form by

$$C_i = \frac{F_i}{\frac{1}{2}\rho A V_\infty^2} \quad \text{with } i = x, y, z \,, \qquad (1)$$

where F represents Force, A reference area, ρ air density and V_∞ freestream air velocity. C_x is the drag component, C_y is the sideforce and C_z is the downforce (negative lift). Moments are expressed differently for a clearer understanding of the results obtained. Pitching moment is translated into a percentage of front axle downforce versus total downforce. This balance is associated with stability once the magnitude of front wheel downforce can translate into understeer or oversteer. By performing a moment balance around the front wheels (origin), M_{y_0}, gives rise to the front wheels ratio of downforce,

$$Front \, [\%] = 100 + \frac{M_{y_0}}{WB \times DF} \times 100 \,, \qquad (2)$$

with WB being the wheelbase of the car (distance between the front and rear wheels) and DF the total downforce. The rolling moment can also be expressed as the proportion of load in the outer wheels when compared to the total downforce, by

$$Outer \, [\%] = \frac{M_{x_0}}{(T \times DF) + 0.5} \times 100 \,, \qquad (3)$$

being M_{x_0} the roll moment around the car centre and T the track width. The last variable in study is the yawing moment coefficient, that is calculated with

$$C_{M_z} = \frac{M_z}{\frac{1}{2}\rho A b V_\infty^2} \,, \qquad (4)$$

where M_z is the yaw moment. These dimensionless coefficients are also displayed multiplied by the reference dimensions in a way that does not mislead conclusions and forces/moments can be easily obtained when multiplying by the dynamic pressure. For example $C_L.A$ and $C_{M_z}.A.b$ where A and b are reference area and length respectively.

3. Implementation

Two models were implemented: CFD simulations were performed to estimate the variables of interest for a particular attitude and a surrogate model as an approximate model that reproduces the behaviour of the simulation model. In this Section, both of these models are described.

3.1. CFD

CFD simulations were more focused on cornering condition because it is the most frequent situation of a Formula Student car. This enabled to gather more information about this type of simulation and it was also chosen to estimate the numerical error associated with it. The software used to perform these simulations was *Simcenter Star-CCM+®*. The geometry in study was prepared to get a clean and simplified geometry for mesh generation and with the intention to parameterize and speed up the interaction between CAD and CFD. Suspension motion and tire shape were taken into account to better replicate the car motion with attitude change.

3.1.1 Cornering Simulation

In a steady-state corner, the vehicle is turning with a constant radius. To model this situation in a CFD simulation, it is imposed an angular velocity to the air and in order to align with free-stream orientation, the domain takes a shape of a partial hollow cylinder (or a donut sector) illustrated in Figure 2 together with the boundary conditions used.

Figure 2: Boundary conditions - corner condition

The geometry was cleaned up using a feature called *Surface Wrapper* and then a Polyhedral Mesher was used to get a discretized representation. Polyhedral mesh increases the number of surface cells for each volume cell increasing the number of neighbour cells, allowing gradients to be more accurately calculated. To refine areas of interest, some boxes were created to efficiently control the cell size. These areas of interest are mainly to capture the car wake and the developed flow structures. The three wake region refinement boxes are displayed in Figure 3 but there are two additional boxes closer to the car, to capture the flow around the front wing and downstream of it, around the lateral diffuser.

Figure 3: Refinement boxes - In farfield region

A steady-state and incompressible fluid was assumed and the Reynolds-averaged Navier–Stokes equations were solved using a $k - \omega$ SST two-equation, eddy-viscosity turbulence model [5] using a segregated flow solver. The use of a transition model was considered, but it was observed that forces and moments did not show any significant change that justified the increased computational time associated. In the car's frame of reference, while driving steadily in a constant radius turn, both air and ground travel in a rotating motion. To mimic this effect, the whole domain was set into a rotating motion by adding a rotating reference frame. This technique enables the possibility of simulating constant motion with a steady-state model without moving the mesh (stationary mesh). In this work, a reference frame is applied to the whole region of study to simulate corner condition.

3.1.2 Adaptive Mesh Refinement

In an attempt to reduce simulation time by allocating better the mesh refinements, an Adaptive Mesh Refinement strategy was tried. Adaptive Mesh Refinement is a method to adjust mesh size (refine or coarsen) based on a chosen criterion from the solution. This means the refinement occurs during the simulation, updating the mesh depending on the current solution. In this case, the chosen mesh refinement criterion for each volume cell is

$$S(r, \theta, z) = |\nabla \cdot \nabla \underbrace{\left(\frac{p_t - p_{ref}}{\frac{1}{2}\rho(\omega r)^2} \right)}_{C_{p_T}}| \times (ACS)^2, \quad (5)$$

where p_t is the total pressure, p_{ref} reference pressure, ω angular velocity of simulation, r cell centroid radius (distance to rotation axis), C_{p_T} total pressure coefficient and ACS is the adaption cell size in volume mesh. In this study, the objective was to focus cell allocation to high values of the Laplacian of total pressure coefficient. It was opted to use the divergence of a gradient instead of a gradient alone to prevent cells from being allocated in areas with constant/high gradient values that can be easily modelled with fewer cells. This Laplacian value is then multiplied by the cell size to get an influence on the current size and the power of two is a tweaked value to find a good ratio between the Laplacian value and cell size. The total pressure coefficient is calculated with a different dynamic pressure because the freestream velocity is not constant throughout the domain. The better way found to fix this problem was to express linear velocity as a function of angular velocity and corresponding radius with: $V = \omega r$. In Figure 4 it is presented a plane section view at a coordinate $X = 475mm$ (intersecting the front wing), displaying the total pressure coefficient where the cell refinement around the vortices structures is visible.

Figure 4: Adaptive mesh refinement C_{p_T}

This strategy was applied to a high-speed corner attitude yielding similar results but still with

3

an increased computational time due to the additional calculations and mesh division during solver. It was then tried in a low-speed corner attitude, but it was not successful. Mesh size increased and fully converged simulation could not be achieved. It was found the best option to discard adaptive mesh refinement and carry the work with the traditional refinement boxes approach.

3.1.3 Tools

Cornering type simulation was analysed in more detail but more types of simulations were performed in this work, namely straight line symmetrical and side wind simulations. These simulations were particularly helpful for parametric studies where each parameter of study was isolated. There is a case where a symmetric condition can be assumed. When the turning radius (R), ϕ, ψ, δ_i and δ_o are null, it is expected that the solution is approximately symmetric from one side of the vehicle to the other. Taking advantage of this condition, the domain of study can be cut in half, reducing the computational time by only studying half of the car. There are other attitudes corresponding to a straight line case $(R = 0)$ that are not symmetric. These conditions will be addressed in this Section. In a straight line scenario, if either roll or yaw angles are different from zero, then a full car simulation must be done. Although roll angle is not usually associated with straight line cases, it was useful to include for parametric studies. These two straight line scenarios have a similar implementation with a rectangular shape domain in CFD and reference frame approach does not apply.

The final step of a CFD simulation workflow post-processing provides tools to analyse and understand the causes of the obtained results. Several pre-checks and monitors were exported during simulation to verify if the setup is correct and to track convergence. Post-processing images included a legend to provide additional information about the simulation setup as displayed in Figure 5.
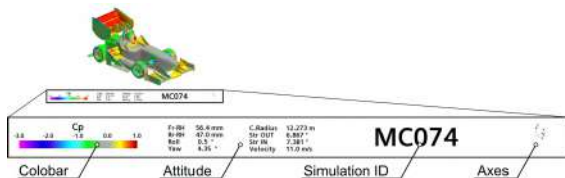
Figure 5: Legend structure of exported images

The CFD simulation workflow was automated to avoid a large amount of repetitive tasks, that are prompt to user error and are time consuming. A macro was created using *Java* programming language that included all three types of simulation from pre-processing up to exporting the results in a CSV format file and post-processing data. An additional macro was also written to gather all the data resulting from CFD in one organized Excel sheet for easy access when needed.

3.2. Surrogate Model

This work aims to evaluate the aerodynamic performance of a prototype as a function of five variables. As the response is found over time-consuming CFD simulations, it was opted to build a surrogate model that reproduces the behaviour of the simulation model. This enables a better understanding of the response over the gaps left from the finite number of simulations in a more rapid and effective manner. Constructing an approximate model requires three steps: design of experiments, construction of the model itself and its validation.

3.2.1 Design of Experiments

The surrogate model used in this work is based on design space approximation in which the interest is only in the overall behaviour of the system throughout the design space [6]. A surrogate model $\widehat{f}$ attempts to mimic the response of the "exact" model f, focusing on understanding the input-output behaviour. To cover the entire design space with discrete points, it requires choosing a sampling plan $\{\mathbf{x}^{(1)}, \mathbf{x}^{(2)}, \ldots, \mathbf{x}^{(n)}\}$ that establishes an efficient spatial arrangement between samples for evaluation through CFD simulations. Finding the input variables at each point in the input space [7] is the first step of the surrogate model, called design of experiments (DOE). The interest while choosing a sampling plan is to minimize the bias error. This error quantifies the extent to which the surrogate model outputs $\hat{f}(x)$ differ from the true values $f(x)$ calculated as an average over all possible data sets D. Each data set D corresponds to a random sample of the function of interest [7]. Besides the bias error, the empirical error also includes a variance component that measures the extent to which the surrogate model $\hat{f}(x)$ is sensitive to a particular data set D. Assuming that the data set includes some type of noise or random element for an average error with a quadratic loss function, the expected error for bias and variance can be expressed as

$$E_{\text{bias}^2}(\mathbf{x}) = \left\{ E_{\text{ADS}}[\hat{f}(\mathbf{x})] - f(\mathbf{x}) \right\}^2, \qquad (6)$$

$$E_{\text{var}}(\mathbf{x}) = E_{\text{ADS}} \left[\hat{f}(\mathbf{x}) - E_{\text{ADS}}[\hat{f}(\mathbf{x})] \right]^2, \qquad (7)$$

where E_{ADS} is the expected value considering all possible data sets. In this work it was implemented a Latin Hypercube sampling (LHS) [8] strategy that

4

decreases both error components. Latin Hypercube sampling is a stratified sampling approach with the restriction of each input variable ($\mathbf{x_k}$) having all portions of its distribution represented by input values [7]. Sampling is done by dividing the range of each design variable $\mathbf{x_k}$ into N_s (sample size) strata of equal marginal probability $1/N_s$, and sample once from each stratum.

3.2.2 Construction of Model

The surrogate model was constructed using a Polynomial Regression Model (PRG) [9] to capture the global behaviour between input and output and due to its simple implementation. PRG is a technique that implements a regression analysis (ence its name) to obtain an estimated value for the function of interest f, based on N_{PRG} number of basis functions z_j, with their respective coefficients β. This approximation of the function is essentially a Taylor series expansion and different values for the order of the polynomial m were tested. For example, considering $m = 1$, this method expresses the linear equation for each sample i and basis function j

$$f_i(\mathbf{z}) = \sum_{j=1}^{N_{\mathrm{PRG}}} \beta_j z_j^{(i)} + \varepsilon_i, \quad E(\varepsilon_i) = 0, \quad V(\varepsilon_i) = \sigma^2, \tag{8}$$

where the error ε_i is assumed to be independent of the sample number with the expected value to be null and variance being σ^2. Representing the first part in matricial form we obtain

$$\boldsymbol{f} = \boldsymbol{X}\boldsymbol{\beta} + \varepsilon. \tag{9}$$

The vector $\hat{\boldsymbol{\beta}}$ containing the unknown parameters can be estimated by

$$\hat{\boldsymbol{\beta}} = \left(\boldsymbol{X^T X}\right)^{-1} \boldsymbol{X^T f}, \tag{10}$$

and the surrogate model approximated output can be found by resolving

$$\hat{\boldsymbol{f}} = \boldsymbol{X}\hat{\boldsymbol{\beta}}. \tag{11}$$

3.2.3 Validation of Model

The third step of making a surrogate model is validation, necessary to assess the approximate model quality. This evaluation is possible by estimating generalization error, providing information to make a decision about the best model choice and it was used a Cross-Validation (CV) [7] approach to estimate it. The data is split into a training set that is used to construct the surrogate model and a testing set used to compute the generalization error from the model. CV enables the use of the majority of the data as training set. The data is split into k-subsets meaning that a surrogate is built k times, each excluding one of the subsets from the training data and using it as testing, to validate the model. The surrogate generalization error is then estimated based on the error from each of the subsets surrogate models.

The strategy chosen to select the data subsets was the leave-one out cross-validation method, where k is equal to the number of samples N_s. A surrogate is built $N_s + 1$ times, N_s times to get all subsets into testing once, and one additional surrogate that uses all the data as training. To estimate the generalization error using a mean square error (GMSE) we obtain

$$\mathrm{GMSE} = \frac{1}{k} \sum_{i=1}^{k} \left(f_i - \hat{f}_i^{(-i)}\right)^2, \tag{12}$$

that represents the variation between the function of interest at the test point f_i and the estimated value from the surrogate model that does not include i as training data $\hat{f}_i^{(-i)}$. This generalization error was calculated for each function of interest and for all orders of the polynomials to provide information to make a founded conclusion on which order suits the problem best.

4. Results
4.1. Numerical Error
To draw more founded conclusions when analysing the results and choose the best mesh size, the numerical error derived from the models used to solve this problem was estimated. The discretization error is typically the greatest source of error and it is assumed to have a predominant effect [10] over the others (round-off, discretization, statistical sampling and iterative errors [11]). The discretization error can be estimated based on a mesh convergence study where results are obtained for different values of mesh spacing parameter, h. This study was performed in a low-speed corner attitude (A1) and then repeated for high-speed corner (A2) displayed in Table 1.

Table 1: Simulation attitudes

	A1	A2
Fr-RH [mm]	38.0	38.0
Rr-RH [mm]	58.0	58.0
Yaw [º]	3.0	3.0
Roll [º]	1.0	1.0
Steer avg [º]	12.0	6.25
Turn Radii [m]	9.125	20.0

The approach used to estimate the error was

based on a power series expansion [12], with three different mesh sizes for each attitude. In Fig.6 the results obtained for each simulation are displayed, together with the best fitting curve for the downforce coefficient.
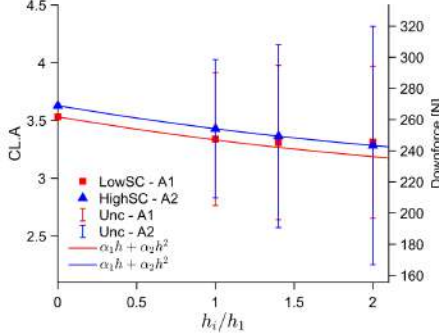

Figure 6: Numerical error estimate for low and high-speed corner attitudes for $C_L.A$

In Table 2 the respective error and uncertainty for $C_L.A$ are summarized with ϕ_0 being the guess of exact solution, ϵ_ϕ the error for null cell size and U_ϕ the uncertainty.

Table 2: Numerical error and uncertainty for $-C_L.A$

	Error		Uncertainty
	ϕ_0	ϵ_ϕ	U_ϕ
A1	3.5317	0.22264	0.66791
A2	3.6282	0.26393	0.79178

Estimated uncertainty and error were proven to have a considerable value due to non-monotonic behaviour and still significant result variation between the different mesh sizes. As this work is mainly based on trends, practically the same conclusions can be drawn while using $h = 1.4$ with a cheaper computational cost. The option chosen for this work was to use $h = 1.4$ for the remaining work, having in mind the respective error and uncertainty.

4.2. Parametric studies

A parametric analysis is performed to evaluate the influence of each parameter of interest on the results. A baseline setup was chosen as a starting point for comparison with $Fr - RH = Rr - RH = 40mm$, $\psi = \phi = \delta = R = 0$ and car velocity of $11.0m/s$.

4.2.1 Ride Height

As front and rear ride heights are connected to each other they are analysed together. A sample selection was needed to cover the entire envelope of ride

heights and spacing of ten millimetres was chosen to evenly distribute the samples, totalling in thirty-five simulations. All points correspond to symmetrical studies, speeding up this process. The results obtained for $-C_L.A$ are shown in Fig. 7 The baseline (FRH40-RRH40) is coloured in white and then increase/decrease is represented in green or red.
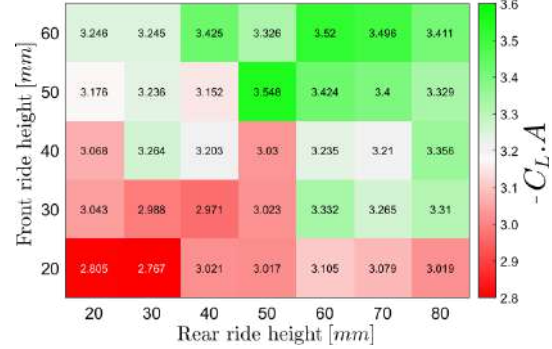
Figure 7: $C_L.A$ Results for ride height parametric analysis

There are two distinct areas, one around the bottom left corner in red and at the top right corner in green. Lower values of front and rear ground clearance are associated with lower downforce numbers. Both front wing and lateral diffuser produce less downforce with lower ride height. Front wing footplate vortex does not form when closer to the ground and the diffuser seems to reach the point where downforce starts to decrease with lower distances to the ground [13]. The same overall trend can be found in the C_D due to the induced drag generated by downforce. The aero balance response was different. On the left side region in Fig. 8 the balance shifts backwards, while on the right side has more downforce on the front wheels.
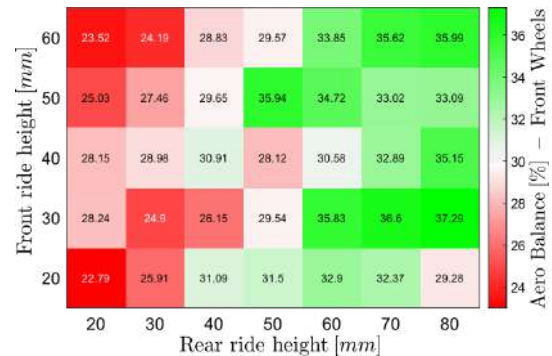

Figure 8: $Balance~[\%] - Front$

4.2.2 Roll Angle

From this study is possible to conclude that $C_D.A$ and $C_L.A$ have a downward trend with increasing roll angle that is displayed in Fig. 9. An abrupt

drop in front downforce is present when reaching one degree and is caused once again by the footplate vortex bursting on the outer side of the vehicle when the front wing gets closer to the ground.
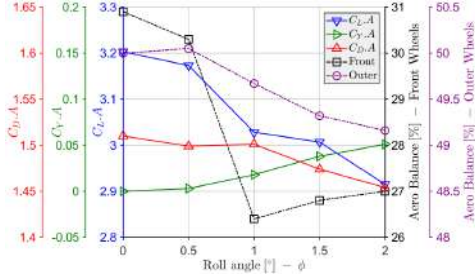

Figure 9: Roll angle parameter study

4.2.3 Steering Angle

The third variable was the steering angle and a bit unexpectedly, it revealed minor changes in $C_L.A$ and $C_D.A$ shown in Fig. 10. Nonetheless, there were some other different important phenomena captured: a substantial increase in side force, aero balance shifting outwards by almost four percentage points. The major change was the rise in yaw moment C_{Mz} showing a linear decreasing trend throughout the entire steering range. This moment always increases in magnitude (with a negative sign) and, as z-axis points upwards, it induces an understeer behaviour to the car.
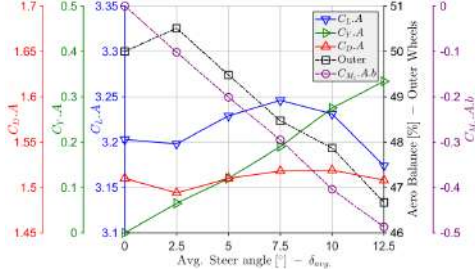
Figure 10: Steering angle parameter study

4.2.4 Yaw Angle

The yaw angle exhibited a large interval of results that are displayed in Fig. 11, having the most impact of all variables in drag and side force coefficient. $C_L.A$ consistently decreased within the interval $[-3.203, -2.674]$ presenting the largest delta of sixteen percentage points, and reached the maximum value for outside load. The front wheel load is the only parameter behaving in a non-monotonic way, starting to drop down but, after $\psi = 7.5°$, it raises up.
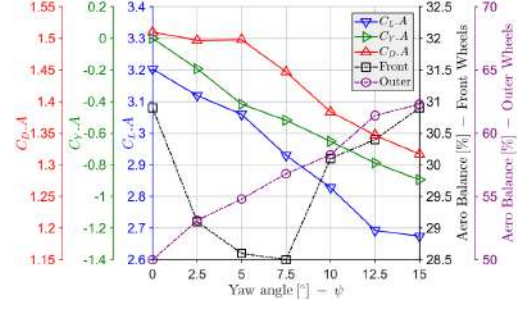
Figure 11: Yaw angle parametric study

4.3. Surrogate Model

The surrogate model was implemented for $m \in \mathbb{N}$, $m \in [1, 12]$ and computing the GMSE by cross validation for each order. The results obtained from the regression analysis were consistent throughout all functions of interest having the polynomial of order two the smallest GMSE in all cases meaning that a polynomial expression was found for each variable of interest with 21 coefficients. The GMSE obtained for the best order is shown in Table 3.

Table 3: GMSE of surrogate model

	GMSE
$-C_L.A$	0.0131
$C_D.A$	0.0006
$C_Y.A$	0.0011
$[\%]\,Out$	0.6979
$[\%]\,Front$	6.0992
$C_{Mz}.A.b$	1.10e-04

Overall the mean square error does not present considerable high values. The front wheel balance and downforce coefficient seem to be more difficult to predict, which is also related to higher oscillations and non-monotonic behaviour noticed during parametric studies.
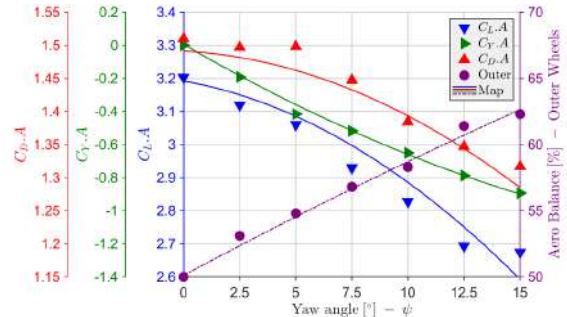

Figure 12: Surrogate model results for Yaw angle ψ parametric studies

In Fig. 13, it is possible to see some overall resemblance to Fig. 7, where warmer colours (higher

values) are positioned at the top right corner and cold (lower values) at the bottom left, meaning the global ride height response seems to be similar. Regarding the other two variables, it is possible to check the different behaviour of the roll and steer based on the ride height in study, both in magnitude and shape. The bottom left peak has an almost circular shape while the top right, the peak moves to the left and resembles more like an ellipse.
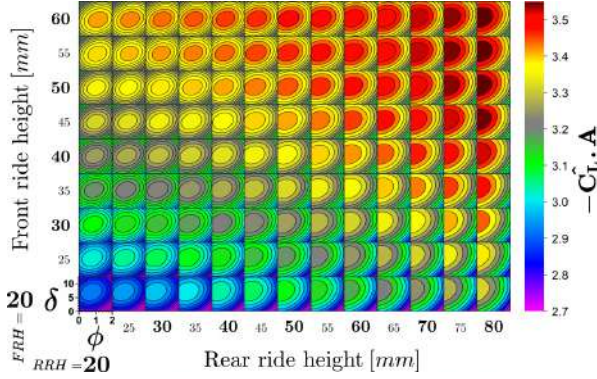

Figure 13: Estimated $-C_L.A$ for $\psi = 0.0°$

Looking at Fig. 14, it is noticeable that the response to ride height looks completely different than before. The model predicts higher values of downforce at the bottom right area for a high value of yaw angle.
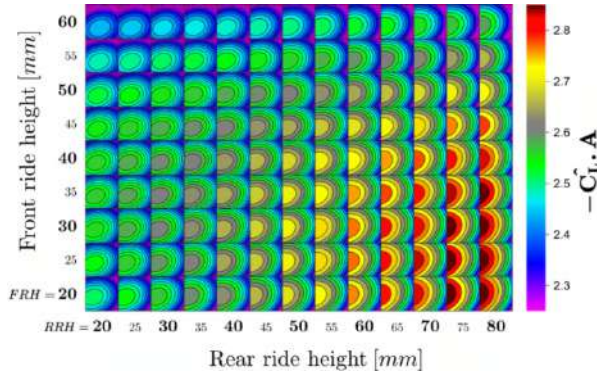
Figure 14: Estimated $-C_L.A$ for $\psi = 15.0°$

5. Validation
Aerodynamic validation was performed to find some correlation between on-track testing and CFD results, allowing to obtain a comparison between the two. The goal of these track tests is to primarily focus on trends between different setups and not on absolute values due to the uncertainties and limited resources and conditions available to achieve it.

5.1. Constant Speed
A constant speed test was carried out in order to estimate the downforce produced by measuring the

suspension deflection. The linear potentiometers located at each spring on FST10e were used to measure the spring displacement due to the downforce generated. By measuring suspension positioning it was also possible to estimate the dynamic ride height using a suspension kinematics and tyre models. It was assigned a number for each attitude, but the numeration does not match the test sequence. This order was chosen to separate the wind direction runs. From 1-3, the test has tailwind and 4-6 headwind. This mixing could mislead to wrong conclusions coming from the simplistic way that the wind problem was solved, besides the fact wind is gusty inducing even more error from this component. The results are illustrated in Fig. 15 including uncertainty bars. As the wind speed inaccuracy exceeds greatly all other sources of error, the experimental uncertainty was estimated by the change in the downforce coefficient with and without a wind component, being approximately 1.0 change in $C_L.A$.
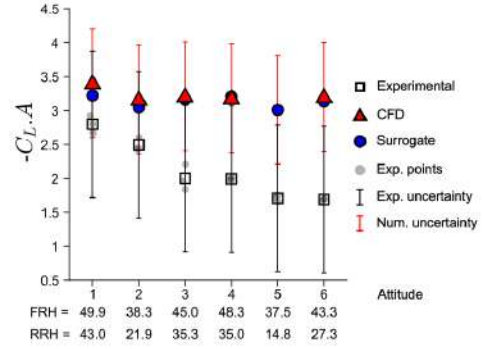

Figure 15: $-C_L.A$ results from constant speed test

Overall, what stands out is the significant difference between experimental and numerical results across all attitudes. The gap is smaller in the first two attitudes but is still significant. The uncertainty magnitudes have proven to be massive, meaning that even if some trend seems to be captured it may be misleading. Analysing the first 3 attitudes (tailwind conditions), the decreasing trend and magnitude change between 1 and 2 looks similar in CFD and on-track but it does not apply to attitude 3, diverging from one other. Looking at the headwind conditions, a similar behaviour occurs, with the decreasing tendency from 4 to 5 resembling the track results (even though with a greater change) but then attitude 6 downforce remains constant, while CFD results points to an increased value. Attitudes 3 and 6 correspond to the runs executed at the end of the day after a few hours have passed and may have been submitted to different conditions. As all the data is averaged across the time interval with constant speed, there

are some variations over this time, mainly related to the car attitude due to bumps on the runway. To better showcase the attitude change over this interval, Fig. 16 displays the averaged standard deviation of ride height for each case.
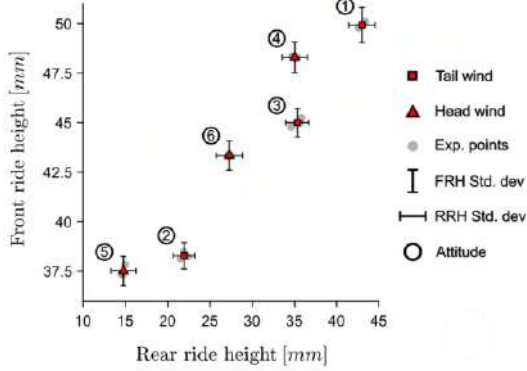

Figure 16: Ride heights and respective standard deviation for constant speed

5.2. Coast Down

The most common way to estimate the drag force is by conducting a coast down test, which consists in accelerating the car up to a certain speed and then coasting. The resistant force responsible for decelerating the car is then determined and can be broken down into several resistance forces components, one of which is the aerodynamic drag. To estimate the drag coefficient of a car, it is necessary to obtain a quadratic function between acceleration and speed during coast down [14]. An example of this data is shown in Fig. 17, where the raw data is shown against the parabolic curve with the best fit.
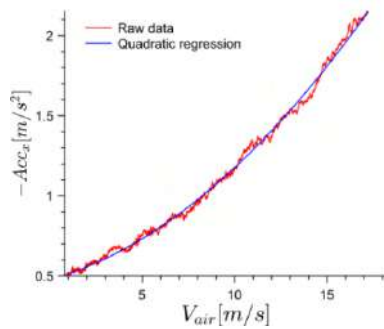

Figure 17: Acceleration vs velocity

The data presents a high level of variation between the same setup runs. The experimental data is presented in Fig. 18 including the results from the surrogate model in the same attitude, uncertainty and standard deviation. The experimental bars represent the $C_D.A$ standard deviation from the 3 sample points ran. The numerical uncertainty

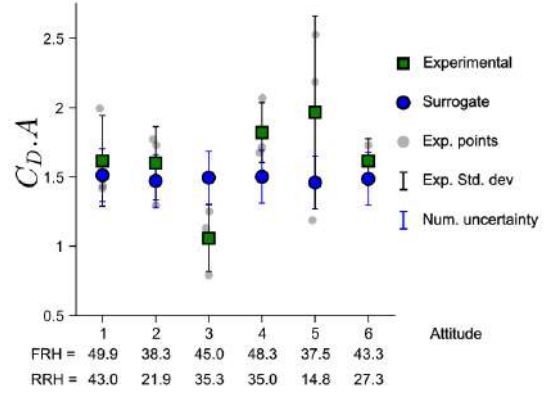represented is the one estimated from the mesh convergence.

Figure 18: $-C_D.A$ results from coast down

Interestingly, there is one experimental point that falls below the surrogate one (attitude 3) which goes against the remaining trend. Usually, it is expected to underestimate the drag due to all the simplifications made in the geometry and conditions of the simulations. Once again, a major source of error may come from the air speed estimation just like in the case of the constant speed test that greatly influences the outcome of these results. It is possible to notice that the change in $C_D.A$ is far greater in experimental results than in numerical. It can be seen that surrogate values barely shift between attitudes. Over this test, both ride heights vary substantially from the beginning to the end, due to the loss of aerodynamic load compressing the suspension. The attitude changes over the course of coast down are shown in Fig. 19. As the rear springs are softer, one would expect the RRH to change the most and that is what happens. In the headwind cases, both ride heights variations are higher reaching a maximum value of 4 millimetres for the standard deviation.
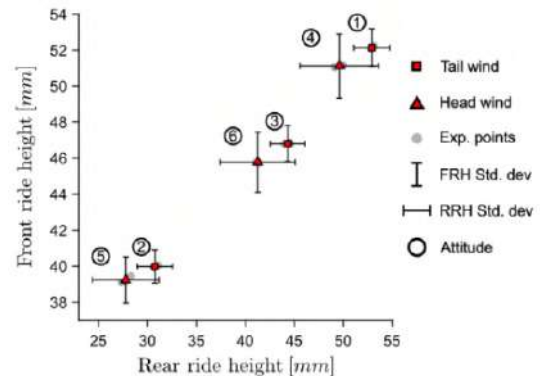

Figure 19: Ride heights and respective standard deviation for coast down

6. Conclusions

During this work, it was possible to notice a change in more than 35% in downforce that confirmed the car behaviour dependence on the attitude and condition proposition for this work. Roll angle revealed to have a monotonic and rather independent behaviour. Ride height presented a significant change in all response coefficients varying by 10% in $C_D.A$ and 20% in $C_L.A$ between peak values, and it was understood that contrary to what was expected, FST10e best working range corresponded to higher ride heights. The steering angle affects the most the yawing moment of the car due to different incidence angles across the car and the yaw angle presented the highest sensitivity to side force coefficient and also a substantial change in drag and downforce. It was also noticed that the downforce coefficient was linked between yaw angle and ride height, meaning that the optimal ride height zone changed based on yaw.

Among the multiple subjects covered in this work, all of them present a large scope for future development. Numerical error and uncertainty from CFD results can be reduced to make more founded conclusions. This can be achieved by increasing cell count or even by further exploring the Adaptive Mesh Refinement methodology. The working range for the parameters of interest can also be extended to incorporate a wider envelope. This applies mainly to yaw angle ψ, where only positive values were taken into account. These are related to oversteer scenarios but understeer conditions with negative yaw angles should be considered in the future. There are more complex approaches that can be used to construct the surrogate model and might find a better response. The surrogate model can be integrated into future vehicle dynamics transient simulators within the team. On-track testing validation is an area of focus that can be greatly exploited. With the possibility to implement further instrumentation on the next prototype, correlation between CFD and reality can be obtained using a quantitative approach estimating the absolute error.

References

[1] William F. Milliken and Douglas L. Milliken. *Race Car Vehicle Dynamics*. SAE International, 1995. ISBN:978-1560915263.

[2] Formula student. `https://www.imeche.org/events/formula-student`, 2022. Online; accessed 2022.

[3] Xin Zhang, Willem Toet, and Jonathan Zerihan. Ground effect aerodynamics of race cars. *Applied Mechanics Reviews*, 59, 01 2006.

[4] Emma Croner, Hervé Bézard, Christophe Sicot, and Guillaume Mothay. Aerodynamic characterization of the wake of an isolated rolling wheel. *International Journal of Heat and Fluid Flow*, 43:233–243, 2013.

[5] F. R. Menter. Two-equation eddy-viscosity turbulence models for engineering applications. *AIAA Journal*, 32(8):1598–1605, 1994.

[6] A. C. Marta. *Aircraft Optimal Design*, chapter Surrogate Models and Multi-Fidelity. Instituto Superior Técnico, Universidade de Lisboa, 2022.

[7] Nestor V. Queipo, Raphael T. Haftka, Wei Shyy, Tushar Goel, Rajkumar Vaidyanathan, and P. Kevin Tucker. Surrogate-based analysis and optimization. *Progress in Aerospace Sciences*, 41(1):1–28, 2005.

[8] M. Mckay, Richard Beckman, and William Conover. A comparison of three methods for selecting vales of input variables in the analysis of output from a computer code. *Technometrics*, 21:239–245, 05 1979.

[9] N.R. Draper and H. Smith. *Applied Regression Analysis*. Wiley Series in Probability and Statistics. Wiley, 1998.

[10] Luís Eça. *Aerodinâmica Incompressível: Exercícios*. IST Press, 1st edition, 2015. ISBN:978-989-8481-33-7.

[11] William L. Oberkampf and Christopher J. Roy. *Verification and Validation in Scientific Computing*. Cambridge University Press, 2010.

[12] L. Eça and M. Hoekstra. A procedure for the estimation of the numerical uncertainty of cfd calculations based on grid refinement studies. *Journal of Computational Physics*, 262:104–130, 2014.

[13] Jonathan Zerihan and Xin Zhang. Aerodynamics of a single element wing in ground effect. *Journal of Aircraft*, 37:1058–1064, 01 2000.

[14] Ion Preda, Dinu Covaciu, and Gheorghe Ciolan. Coast down test – theoretical and experimental approach. In *CONAT 2010 - International Automotive Congress*, 10 2010.